Boron Nanosheets Boosting Solar Thermal Water Evaporation

Xin Stella Zhang, Shudi Mao, Jiashu Wang, Casey Onggowarsito, An Feng, Rui Han, Hanwen Liu, Guojin Zhang, Zhimei Xu, Limei Yang, Qiang Fu * and Zhenguo Huang *

School of Civil and Environmental Engineering, University of Technology Sydney, Ultimo, New South Wales 2007, Australia

Qiang F* (qiang.fu@uts.edu.au), Zhenguo H* (zhenguo.huang@uts.edu.au)

Abstract

Hydrogel-based solar vapour generators (SVG) are promising for wastewater treatment and desalination. The performance of SVG systems is governed by solar thermal conversion and water management. Progress has been made in achieving high energy conversion efficiency, but the water evaporation rates are still unsatisfactory under one sun irradiation. This study introduced novel two-dimensional (2D) boron nanosheets as additives into hydrogel-based SVGs. The resulting SVGs exhibit an outstanding evaporation rate of 4.03 kg m^{-2} h^{-1} under one sun. This significant improvement is attributed to the 2D boron nanosheets, which leads to the formation of a higher content of intermediate water and reduced water evaporation enthalpy to 845.11 kJ kg^{-1}. The SVG incorporated with boron nanosheets also showed high salt resistance and durability, demonstrating great potential for desalination applications.

Introduction

Water scarcity is becoming one of the significant challenges faced by human beings in recent decades. [1, 2] Tremendous efforts have been devoted to seawater desalination and wastewater purification via reverse osmosis to alleviate the shortage of fresh water. However, these technologies still face many challenges, such as sizeable initial investment, high energy consumption for operation, and the negative impact of brine discharge on the environment. Water resources per capita are scarcer in the arid and poor areas of the world today. [3, 4] In this context, solar vapour generator (SVG) [5-9] arouses keen public interest due to its sustainability, low capital investment, and environmental friendliness.

SVG performance is moderated by heat and water management. Photothermal materials can be incorporated into hydrogels to maximise the conversion of solar radiation into heat. Only through solar-thermal conversion the SVG evaporation rate will be limited to a maximum theoretical value of 1.47 kg m^{-2} h^{-1} under one sun radiation. [10, 11] Therefore, water management, in particular adequate water transportation from the source to the evaporation interface, is essential. Hydrogels are of interest because they can swell in water in three dimensions, thus increasing water transport. [12] The structural units of hydrogels can interact with water molecules, i.e., increase the ratio of intermediate to free water and decrease the enthalpy of evaporation, [13] thus increasing the evaporation rate.

Many previous studies have focused on improving thermal management, including developing advanced photothermal materials, [8] constructing rough evaporation interface of hydrogels, [14, 15] improving the light harvest[16] and optimising thermal insulation to reduce heat loss. [3, 17] In particular, two-dimensional (2D) nanomaterials such as graphene oxide (GO), [18, 19] g-C_3N_4[20] and MXene[21] have been incorporated into hydrogels to enhance solar thermal conversion. 2D materials have a great advantage over bulk counterparts because their unique geometry maximises exposure to light and water, which enhances heat production and, hence, water evaporation. Recently, boron nanosheets with various surface configurations have received increasing interest due to their unique photothermal properties and excellent structural and chemical stability. [22-24] The single atomic layer of boron nanosheet, commonly known as borophene, has been grown via epitaxial growth under ultrahigh vacuum (UHV). Borophene is extremely sensitive to air, and its application is therefore very limited. [25-27] Thick boron nanosheets have thus been prepared by exfoliating amorphous and crystalline bulk boron. [28, 29]

In this study, we obtained amorphous (ABNS) and crystalline boron nanosheets (CBNS) with high stability using low-temperature sonication-assisted liquid-phase exfoliation. We then incorporated boron sheets as photothermal materials into a polyvinyl alcohol (PVA) matrix, and the hydrogels were fabricated via a freezing-thawing process (the obtained SVGs were denoted as ABNS/PVA and CBNS/PVA, respectively). The introduction of boron nanosheets not only improves the photothermal conversion efficiency but also effectively reduces the water evaporation enthalpy due to the strong

interaction between CBNS and water molecules. As a result, the resulting CBNS/PVA SVG exhibits an outstanding water evaporation rate of 4.03 kg m^{-2} h^{-1} under one sun with a high solar-thermal efficiency of 94.6%. Moreover, the system exhibited high durability and salt tolerance, making CBNS/PVA a promising candidate for practical applications.

1. Results and Discussion

1.1. Characterization of boron nanosheets

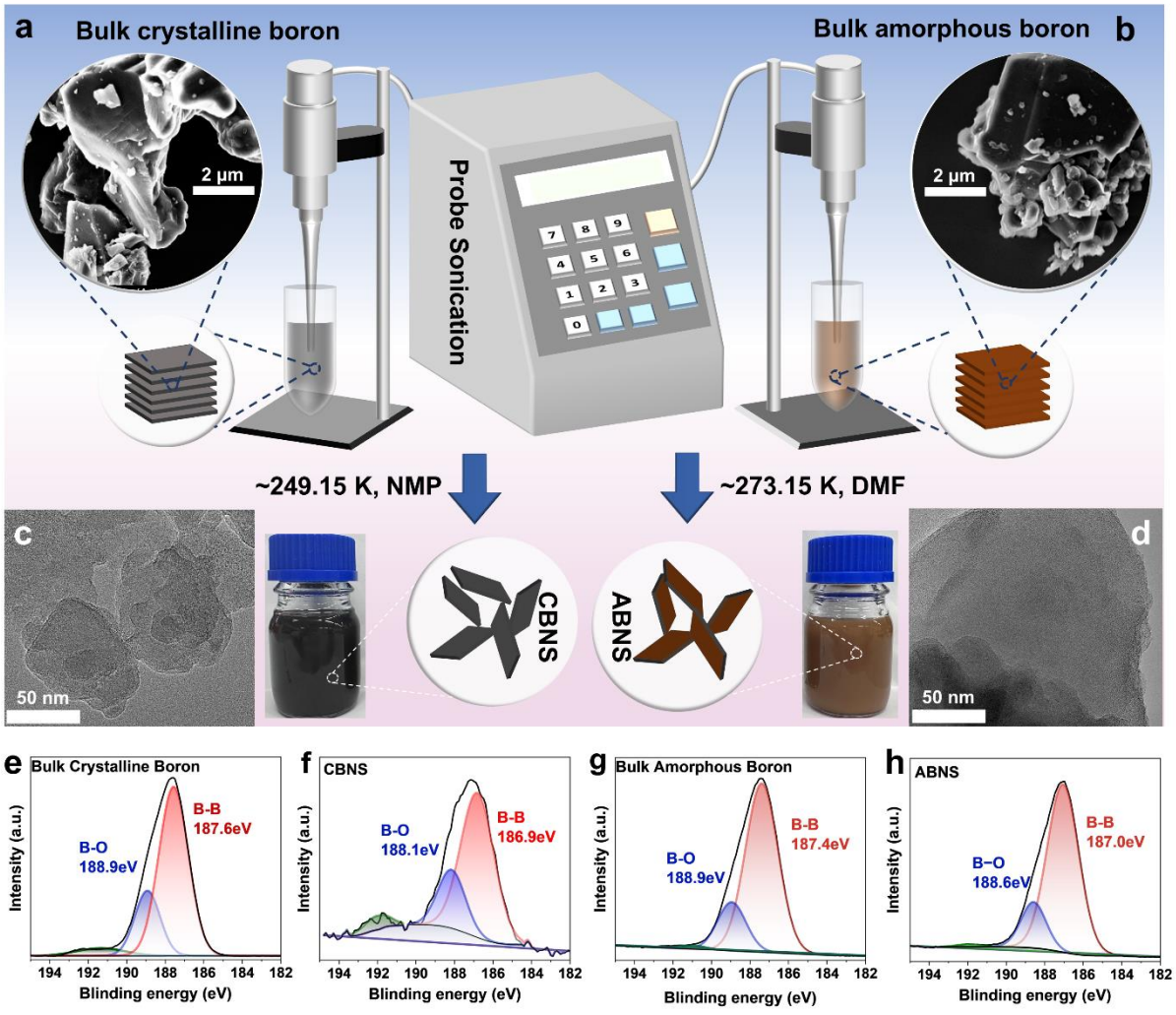

Fig. 1 Schematic illustration of the fabrication of the boron nanosheets, (a, b) SEM image of bulk boron, (c) TEM image of CBNS and digital image of CBNS suspended in NMP, (d) TEM image of ABNS and digital image of ABNS suspended in DMF, B 1s XPS spectra of (e) bulk crystalline boron, (f) CBNS, (g) bulk amorphous boron, and (h) ABNS.

This work employs low-temperature sonication-assisted liquid-phase exfoliation (Fig. 1) to obtain boron nanosheets. First, bulk crystalline boron powders were loaded in 1-Methyl-2-pyrrolidone (NMP) (1 mg mL^{-1}) [29], and the CBNS was then obtained via sonication at 500 W for 12 h in a -24 °C cold bath. Similarly, ABNS was fabricated by sonicating bulk amorphous boron powders in N, N-

dimethylformamide (DMF) (1 mg mL^{-1}) at 500 W for four h in a 0 °C cold bath. [28] After sonication, both mixtures were allowed to stand for 48 h and then centrifuged at 3000 rpm. The supernatants were collected and then filtered through a membrane filter with a pore size of 220 nm to obtain ABNS and CBNS, respectively. These boron sheets were washed with deionised (DI) water three times and dried in a vacuum oven (45 °C, 185 mbar) for 24 h. Transmission electron microscope (TEM) images of CBNS and ABNS are shown in Fig. 1 (c) and (d), respectively. CBNS suspension is black, while ABNS suspension appears brown, as shown in Fig. 1 (c) and (d). Lamellar CBNS and ABNS can be further observed in the scanning electron microscope (SEM), and AFM results of CBNS and ABNS are shown in Fig. S1 and Fig. S2, respectively. These results prove the successful fabrication of nanosheets from bulk amorphous and crystalline boron. The corresponding energy dispersive spectroscopy (EDS) elemental mapping images (Fig. S3 (a)-(b)) show the distribution of B and O elements. The origins of O can be attributed to the oxidation of B, forming B-O bonds and also the adventitious O_2 adsorbed during analysis.

We also investigated the surface composition, chemical state of CBNS and ABNS, and the commercial bulk boron materials by X-ray photoelectron spectroscopy (XPS). The survey scans are presented in Fig. S4. Carbon is commonly observed in XPS due to the chemical nature of adventitious carbon in air. The slightly higher XPS nitrogen peak intensity for the nanosheets can be attributed to the solvent used, N-methyl-2-pyrrolidone (NMP). As shown in Fig. 1 (e)-(h), B 1s profiles of boron sheets and bulk boron can be deconvulated into three peaks, and the main peak around 186.9−187.9 eV can be attributed to B−B bonds. [28-30] After exfoliation, the B−B peaks of ABNS (centred at 187.0 eV) and CBNS (centred at 186.9 eV) are sligtly red-shifted compared to those of the starting materials, which is consistent with previous reports. [27, 31] Peaks centered at around 188 eV and 192 eV can be assigned to the B−O bond in suboxide and B_2O_3, respectively. [28, 30, 31] The compositions of B−B and B−O in suboxide are listed in Table S1. CBNS displays the highest B−O peak intensity (or $I_{B\text{-}O}/I_{B\text{-}B}$) suggesting the highest degree of oxidation. Both CBNS and ABNS have Raman spectra similar to their bulk counterparts (Fig. S5).

X-ray diffraction (XRD) patterns and Fourier transform infrared (FT-IR) spectra were also collected to examine the structure of the nanosheets. XRD patterns of bulk crystalline boron, bulk amorphous boron, CBNS and ABNS are shown in Fig S6 (a)-(b). We observed the characteristic diffraction peaks of crystalline boron (β-rhombohedral, JCPDF No. 04-007-2390), and amorphous boron (JCPDF No. 00-031-0207). [28, 29, 32] In the FT-IR spectra of CBNS and ABNS (Fig. S7 and Fig. S8), the strong IR bands observed in the rang ~1200~1400 cm^{-1} are associated with B–O stretching. [33, 34]

1.2. Fabrication of hydrogels for SVG application

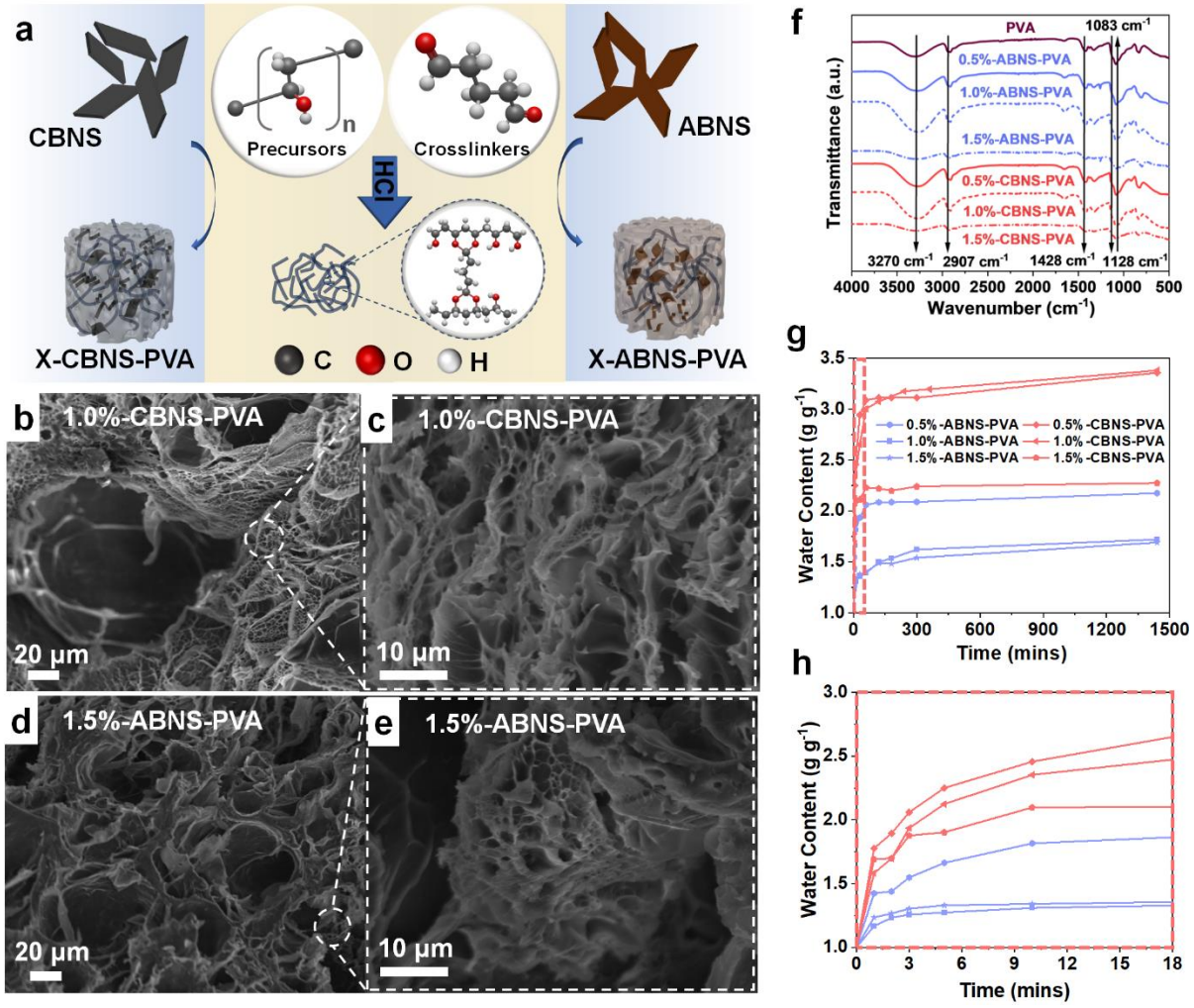

Fig. 2 (a) Schematic illustration of the fabrication of the SVGs. SEM images of (b, c) 1.0%-CBNS-PVA hydrogel and (d, e)1.5%-ABNS-PVA hydrogel. (f) FTIR spectra of x-ABNS-PVA (blue line), x-CBNS-PVA (red line) and pristine PVA (brown line). Water content of the hydrogels plotted against water absorption time within (g) 1440 minutes and (h) 18 minutes.

In this study, both ABNS and CBNS are employed as photothermal materials in PVA hydrogels prepared via a freeze-thaw approach.[35, 36] For comparison, we also prepared hydrogels with GO as the photothermal material. The preparation of SVG is illustrated in Fig. 2 (a). PVA and GA were first dissolved in DI water. Subsequently, a certain amount of photothermal materials (ABNS, CBNS, or GO) was introduced to the solution and sonicated for 30 minutes. A solution of HCl (0.1 M) was added and after 5-10 min the mixture was placed in a freezer at −18 °C overnight. For characterization and water evaporation tests, hydrogels were thawed in DI water at room temperature and freeze-dried for 48 hours. The resultant samples are denoted as *x*-ABNS-PVA, *x*-CBNS-PVA, and *x*-GO-PVA, respectively, where *x* represents the corresponding photothermal materials loading in the hydrogels (0.5, 1.0 and 1.5 wt %). The as-prepared *x*-ABNS-PVA and *x*-CBNS -PVA are brown and black, respectively.

As can be seen from the cross-sectional SEM images (Fig. 2(b)-(e) and Fig. S9), the resulting hydrogels are highly porous with relatively uniform internal pore size. Compared with pristine PVA or 1.0%-GO-PVA hydrogels, x-CBNS-PVA and x-ABNS-PVA have larger pores (Fig. S9 (i)-(j)), which can facilitate water transport in the hydrogels, thus further improving water evaporation rate. The FTIR spectra of x-ABNS-PVA and x-CBNS-PVA are nearly identical to that of pristine PVA sample (Fig. 2 (f)). The broad peak at 3,270 cm^{-1} in all the spectra can be assigned to the stretching of O-H groups of PVA. [3, 35] The IR bands at 2,907, 1,428 and 1,128 cm^{-1} can be attributed to C–H, CH_2 and C–O stretching, respectively. [37, 38] The FTIR spectra of 1.0%-CBNS-PVA and 1.0%-GO-PVA show in Fig. S12, which is similar to that of PVA. UV-vis-NIR spectrophotometer was used to determine the light absorption. All hydrogels, except for bare PVA, exhibit excellent light absorption properties across the entire solar spectrum (300–2500 cm^{-1}) (Fig. S10), which is beneficial for solar thermal conversion.

The hydrogels display different water content and water transport capabilities. The water swelling ratio (Q) of the hydrogels at time 't' was recorded using Eq. 1 [35]

$$Q = \frac{M_t}{M_{dry}} \qquad \text{Eq. 1}$$

The profiles in Fig. 2 (g-h) show the different capabilities of hydrogels to absorb water. They all feature rapid water absorption at the initial stage (t < 3 min) and reach a plateau within 300 minutes. The swelling ratios of the *x*-CBNS-PVA hydrogels are all higher than those of the *x*-ABNS-PVA counterparts, indicating that CBNS has a higher affinity for water. On a particular note, the 1.0%-CBNS-PVA showed the highest swelling ratio of 3.38 g g^{-1} after 24 hours. In contrast, the swelling ratio of pristine PVA is 2.5 g g^{-1} after 24 hours, which is in good agreement with a previous report. [39]

1.3. Intermediate water in the hydrogels

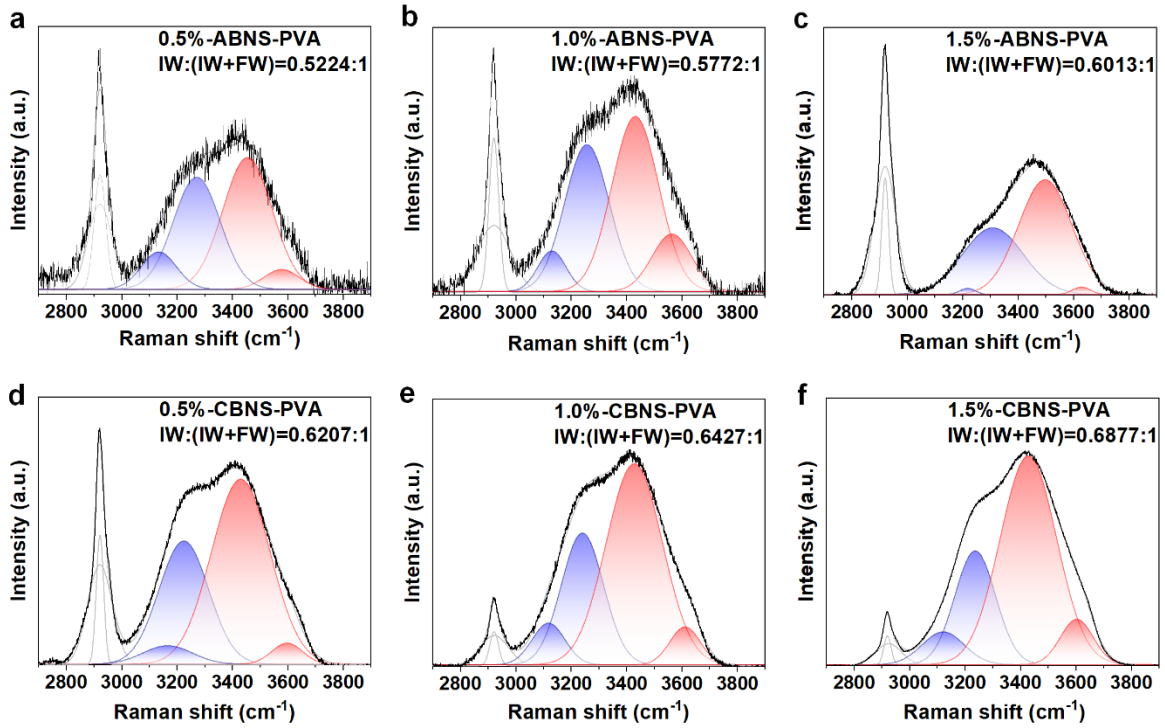

Fig 3. Raman spectra of (a) 0.5%-ABNS-PVA, (b) 1.0%-ABNS-PVA, (c) 1.5%-ABNS-PVA, (d) 0.5%-CBNS-PVA, (e) 1.0%-CBNS-PVA and (f) 1.5%-CBNS-PVA.

According to the literature, water in hydrogels typically exists in three states: "bound", "intermediate" and "free" state.[3] The polymer chains in a hydrogel can trap nearby water molecules through strong interactions such as hydrogen bonding to form bound water. Water molecules interacting with bound water are known as intermediate water, which can be evaporated by less energy compared with bound water and free water. [3, 6, 40] Hydrophilic functional groups (i.e. –COOH, –OH, –NH_2, etc.) on polymer chains have been found to affect the formation of IW. [3, 40] An effective way to improve water management and boost evaporation rates in hydrogels is to increase the IW content[3, 4, 35] because IW molecules usually display lower evaporation enthalpy. [3, 36] Raman spectroscopy analysis can be employed to determine the IW contents in the hydrogels (Fig 3). After peak fitting, we can clearly distinguish the FW (blue traces) and IW (red traces) peaks in the Raman spectra. The *x*-CBNS-PVA hydrogels have higher IW/(IW+FW) ratios than those of *x*-ABNS-PVAs and the GO-PVA hydrogel (Fig. S11, IW/(IW+FW) = 0.5035). The high IW contents are likely due to the higher degree of oxidation of CBNS. Based upon the XPS results, compared with ABNS, there are more B-O bonds in CBNS, which leads to more hydrogen bonding with water molecules and, therefore, a higher portion of IW.

1.4. Solar-vapour generation performance

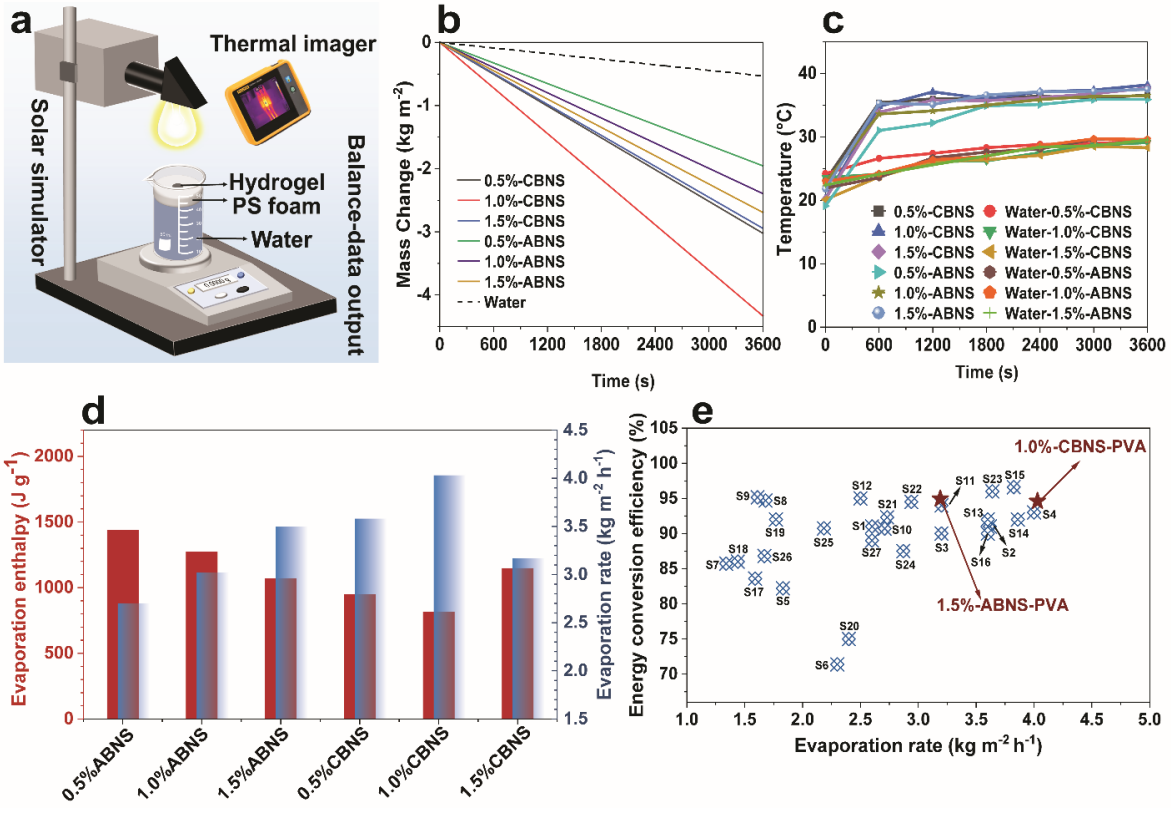

Fig. 4. (a) Schematics of the SVG setup under one sun irradiation, (b) water mass changes during SVG measurements where a linear fit has been presented, (c) temperature changes of x-ABNS-PVA and x-CBNS-PVA hydrogels, with and without water; (d) equivalent evaporation enthalpy and evaporation rate of x-ABNS-PVA, x-CBNS-PVA; (e) comparison of SVG performance among various hydrogels (references shown in Table S1).

Water evaporation performance[41] was assessed using a custom-built setup under a solar simulator (Oriel LCS-100 Small Area Sol1A) to generate one sun irradiation (Fig. 4 (a)). The solar irradiance on the surface of the hydrogel was calibrated to be one sun using a portable power and energy meter console (PM100D, Thorlabs, Germany). Hydrogels were fixed at the centre of a polystyrene (PS) foam, with the bottom of the hydrogels maintaining contact with water and the top facing the light bulb. To minimise natural water evaporation, sealant was applied between the PS foam and the beaker to seal the gaps. Every 30 seconds, mass was recorded on an electronic mass balance (KERN TALJG 220-5-A). A layer of PS foam was also placed between the beaker and the mass balance to provide thermal insulation. The data were calibrated by subtracting the mass loss under dark conditions. During the solar vapour generation tests, a Fluke PTi120 pocket thermal imager was used to record the surface temperature of the hydrogel and the bulk water.

As shown in Fig. 4 (b), a linear fitting can be used to estimate the evaporation rates based on the slopes of the mass-time curve, and the mass loss rates for *x*-CBNS-PVA and *x*-ABNS-PVA are *ca.* 5 to 9 times higher than that of natural water evaporation under the same conditions, respectively. The 1.0%-CBNS-PVA displayed the best performance with an evaporation rate of 4.03 kg m^{-2} h^{-1}.

Incorporating 2D boron nanosheets as photothermal materials into PVA hydrogels can increase the temperature of the evaporation interface. After 60 minutes of irradiation, the temperatures of dry CBNS and ABNS powders reached 55.5 °C and 56.6 °C, respectively, suggesting an excellent solar thermal conversion (Fig. S13). For the hydrogels with boron nanosheets, elevated temperatures of 32–39 °C were observed at interfaces after 10 minutes of irradiation (Fig. 4 (c)), higher than the temperature of bulk water (around 22 °C). Records of temperatures and the infrared images are listed in Fig. S14-16 and Table S2. The experimental results show that CBNS demonstrates a higher photothermal conversion efficiency compared to ABNS. As a result, the temperature difference between the evaporation interface and bulk water is more remarkable for CBNS/PVA than for ABNS/PVA. Due to the existence of IW, the vaporisation enthalpy for water in the SVGs is much lower than that of FW. Water vaporisation energy measurements were carried out with a 20 mL/min nitrogen flow rate over a temperature range of 20 to 200 °C with a linear heating rate of 10 K min^{-1}. The equivalent evaporation enthalpies and the evaporation rates of these SVGs can be found in Fig. 4 (d), Fig. S17 and Table S3,4. The equivalent enthalpy of 1.0%-GO-PVA is higher than *x*-CBNS-PVA. This can be attributed to the bond polarity difference between C–O in GO and B–O in CBNS, which affects the hydrogen bonding within the hydrogels and, consequently, water evaporation enthalpy. The equivalent evaporation enthalpy for 1.0%-CBNS-PVA was found to be 845.11 kJ kg^{-1}, the lowest among all the hydrogels, which can be attributed to its high IW/(IW+FW) ratio of 0.6427 and a high-water content of 3.38 g g^{-1}. The equivalent evaporation enthalpy of pristine PVA hydrogel was 1,483.95 kJ kg^{-1}. Zuo et al. [7] studied the mechanism of the metallic λ-Ti_3O_5 exciting water molecules (i.e. H_3O^*) at the evaporation interface. Chen et al. [42] introduced a photo-molecular effect where photon can cleave off water clusters at the liquid water–vapour interfaces. For both studies, the formation of intermediate water plays a key role. In this study, the high evaporation rate can be attributed to the high content of intermediate water produced in the hydrogel.

The solar-to-vapour efficiency was calculated using equation 2[3, 4, 35, 43]

$$\eta = \frac{\dot{m} \times h_v}{C_{opt} \times P_0} \qquad \text{Eq.2}$$

Where $\dot{m}$ is the evaporation mass flux (water evaporation rate); h_v refers to water equivalent evaporation enthalpy; C_{opt} is the optical concentration on the absorber surface (calibrated to be 1 using an energy meter console), and P_0 refers to the solar irradiation power (1 kW m^{-2}). The conversion efficiencies, evaporation rates and equivalent evaporation enthalpy are shown in Table S2. Significantly,

solar to vapour efficiencies of *x*-CBNS-PVA and *x*-ABNS-PVA are above 75%. We compared the water evaporation performance of the 1.0%-CBNS-PVA and 1.5%-ABNS-PVA with the state-of-the-art SVG systems (Fig. 4 (e) and Table S6). To ensure a fair comparison, we only consider energy efficiency and evaporation rates for SVGs using a similar experimental setup, thus excluding the 3D SVG systems. [44] For instance, Lu *et al.* recently reported the development of few-layered $Ti_3C_2T_x$ MXene/rGO hydrogels, which showed excellent evaporation rates up to 3.62 kg m^{-2} h^{-1} and a great efficiency of 91%.[15] Yu *et al.* also developed a patchy-surface hydrogel PVA/OTS/Ti_2O_3 and achieved an evaporation rate of 4.0 kg m^{-2} h^{-1} with an efficiency of 93%.[45] To the best of our knowledge, the present 1.0%-CBNS-PVA displayed the highest water evaporation rate with a high energy efficiency of *ca.* 94.6% compared to state-of-the-art PVA-based SVGs. This result can be attributed to the fact that the 1.0%-CBNS-PVA simultaneously exhibited a high IW content as well as the highest swelling ratio. In contrast, although 1.5%-CBNS-PVA displayed the highest IW/(IW+FW) ratio, its swelling ratio is relatively low. Particularly, given the relatively low interfacial temperature of the x-CBNS-PVA SVG and its paradoxically outstanding evaporation rate, it is evident that the incorporation of boron nanosheets contributes significantly to the generation of a high IW content, which reduces the enthalpy of evaporation. When we further increased the surface area of the 1.0%-CBNS-PVA hydrogel to 10 cm^2, we observed a decrease in the water evaporated rate to 3.60 kg m^{-2} h^{-1}. This result agrees with the previous report that increasing the surface area resulted in a decrease in the evaporation rate. [46] This phenomenon can be attributed to the lack of convective coverage in the central region of the large surface to carry away the accumulated water vapour.

3.5 Seawater distillation

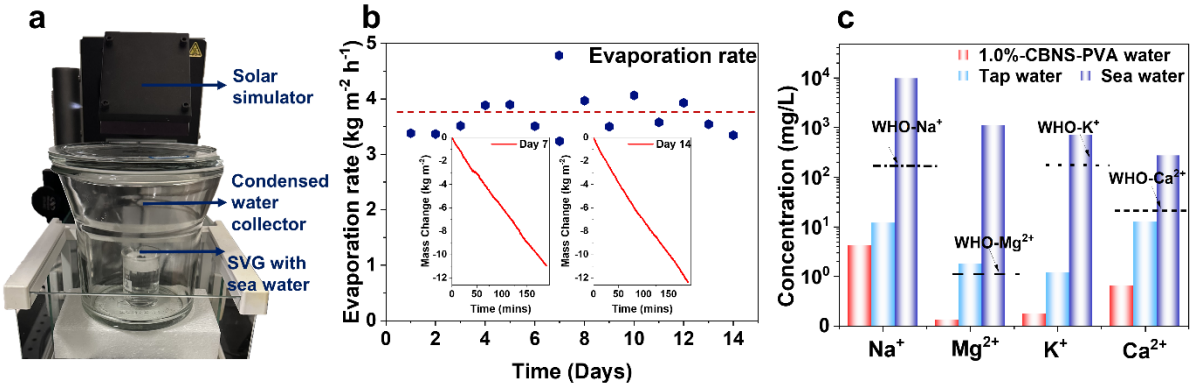

Fig. 5 (**a)** Setup for seawater SVG and condensed water collection; (b) evaporation rates of 1.0%-CBNS-PVA immersed in seawater for two weeks; (c) concentrations of the four major ions (Na^+, Mg^{2+}, K^+, Ca^{2+}) measured in purified water evaporated by 1.0%-CBNS-PVA, normal tap water and seawater in Sydney (Australia).

Finally, we evaluated the seawater (salt concentration = 400 g L^{-1}) desalination performance of the 1.0%-CBNS-PVA hydrogel using the setup illustrated in Fig. 5 (a). To collect desalinated seawater, a

container was used that allowed solar light to pass through completely, and the water steam condensed on the glass wall. The evaporation rates were measured after every three hours during the day for fourteen days. As shown in Fig. 5 (b), the evaporation rates of 1.0%-CBNS-PVA remained around 3.62 kg m^{-2} h^{-1} during the desalination test, and no significant salt accumulation was observed after long-term testing (Fig. S18 in Supplement Data). After each desalination cycle, the hydrogel was left sitting in the water for 3 hours, during which all the salts were redissolved entirely in the water. Inductively coupled plasma mass spectroscopy (ICP-MS) analysis showed that the ion concentrations (i.e. Na^+, Mg^{2+}, K^+, Ca^{2+}) of the desalinated water by 1.0%-CBNS-PVA were reduced significantly by 2 to 3 orders of magnitude (Fig. 5 (c)), far exceeding the world health organisation (WHO) [47, 48] drinking water standard. These results thus demonstrate the high durability, high salt tolerance and high desalination performance of the CBNS-PVA evaporator.

2. Conclusion

In this study, we prepared few-layered boron nanosheets by exfoliating bulk crystalline and amorphous boron powders. By incorporating the nanosheets into PVA-based hydrogels, we developed highly efficient SVG systems with high water evaporation rates of up to 4.03 kg m^{-2} h^{-1} and 94.6 % solar-to-vapour efficiency. The system also has excellent salt tolerance in solar-driven seawater evaporation. The outstanding performance of CBNS-PVA hydrogel for solar vapour generation can be attributed to the 2D geometry with high oxidation, high IW content and low enthalpy of water evaporation, which together lead to high solar thermal conversion and water management simultaneously. This work demonstrates the great potential of boron nanosheets for practical SVG applications. It also suggests that developing novel additives to reduce water evaporation enthalpy will be highly beneficial in achieving more cost-effective water production.

3. Materials and Method

3.1. Materials

Amorphous boron powders (⩾95%), crystalline boron powders (⩾99%), N, N-dimethylformamide (anhydrous DMF, 99.8%), graphene oxide (GO, 4–10% edge-oxidized), polyvinyl alcohol (PVA, MW 89000-98000) and glutaraldehyde (GA, 25% aqueous solution) were purchased from Sigma-Aldrich. 1-Methyl-2-pyrrolidone (NMP, 99.9%) was purchased from Supelco. All materials were used as received without any further purification.

3.2. Sample preparation

4.2.1 Preparation of ABNS

100 mg of bulk amorphous boron powders were added into 100 mL of DMF. The mixture was sonicated at 500 W for 5 h, with 5 s operation and 2 s pause on a probe ultrasonic processor (VCX 500, Sonics &

Materials, Inc), cooled by a nitrogen gas stream. The sample container sat in a 0 °C ice bath and was sealed with Teflon tape to minimise air exposure during the ultrasonic process. After resting at room temperature for 48 h, the supernatant was decanted and centrifuged at 3,000 rpm for 9 min to remove large bulk amorphous boron powders. The suspension was then vacuum filtrated through a membrane with 220 nm pore size to obtain solid products. The ABNS powders were finally dried at 45 °C in a vacuum oven for 48 h.

4.2.2 Preparation of CBNS

30 mg of crystalline boron powders were added into 30 mL of NMP to form a suspension by stirring. The container with the mixture was placed in a glycol cold bath at −24 °C and then sonicated at 500 W for 12 hours, with 4 s operation and 2 s pause using the probe ultrasonic processor. The CBNS powders can be obtained via the same vacuum filtration and drying process.

4.2.3 Fabrication of hydrogels

PVA solution (10 wt%) was prepared by dissolving PVA (MW: 89–98 kDa) in deionised water at 65 °C. ABNS, and CBNS with different weight percentages (0.5%, 1.0% and 1.5%) were added into PVA solutions (10 wt %, 2 mL), respectively. After sonication, GA solution (40 μL, 25 wt % in DI water) and HCl (50 μL, 32 wt %) were added. The resultant mixtures were kept for 2 h and then immersed in DI water overnight. The hydrogels were frozen and then thawed in DI water at 25 °C. After freeze-drying, the prepared *x*-ABNS-PVA and *x*-CBNS-PVA hydrogels were washed with DI water three times. Those gels were then soaked in water at room temperature for at least 4 hours and finally placed into a polystyrene foam for water evaporation performance testing.

3.3. Characterisation

4.3.1 Analytical methods

The morphology and structure of the boron nanosheets were characterised on a transmission electron microscope (TEM, 60-300 kV, Thermo Fisher Spectra), scanning electron microscope (SEM, 5-10 kV, Zeiss Supra 55VP), Bruker D8 Discover X-Ray Diffractometer (XRD), Park XE7 atomic force microscope (AFM), and Thermo Scientific Nicolet 6700 Fourier transform infrared spectrometer (FTIR). The chemical state of boron was determined using ESCAB 250xi X-ray photoelectron spectroscope (XPS, referenced to C 1s at 284.8 eV). Zeiss Evo LS15 scanning electron microscope (10-15kV) was used to study the hydrogel microstructure. Oxford energy dispersive spectroscopy (EDS) was employed to analyse chemical composition. All hydrogels were freeze-dried before SEM imaging. Thermo Scientific Nicolet 6700 FT-IR spectrometer was used to analyse hydrogels. A Renishaw inVia Raman spectrometer system (Gloucestershire, UK) was used to calculate the intermediate water (IW) and free water (FW). Ultraviolet-visible-near infrared (UV-VIS-NIR) spectra of hydrogels were taken in the range of 300–2500 cm^{-1} using Agilent Cary 7000 UMS Universal Measurement Spectrophotometer. The surface temperature was taken by a Fluke PTi120 thermal imaging camera.

The vaporization enthalpy of hydrogels was measured on a SDT Q600 V20.9 differential scanning calorimeter (DSC). Water salinity concentration was analysed with Agilent 7900 ICP-MS.

4.3.2 Water absorption tests

To determine the swelling ratio, after freeze-drying, those hydrogels were first soaked at room temperature for at least 4 hours and then freeze-dried again to obtain the dry state weight (Wdry). To monitor water absorption, soak the hydrogels in DI water for 30 s, 60 s, 2 min, 5 min, 10 min, and 30 min, and then weigh the corresponding mass, respectively.

Conflicts of interest

The authors declare that they have no known competing financial interests or personal relationships that could have appeared to influence the work reported in this paper.

Acknowledgement

Z.H acknowledges support under the Australian Research Council's Discovery Projects funding scheme (project number DP220103458) and the Future Fellowship (FT190100658). Q.F. acknowledges support under the Future Fellowship (FT180100312).

Reference

1. C. He, Z. Liu, J. Wu, X. Pan, Z. Fang, J. Li and B. A. Bryan, *Nature Communications*, 2021, **12**, 4667.
2. A. Dinar, A. Tieu and H. Huynh, *Global Food Security*, 2019, **23**, 212-226.
3. Y. Guo, H. Lu, F. Zhao, X. Zhou, W. Shi and G. Yu, *Adv Mater*, 2020, **32**, e1907061.
4. F. Zhao, X. Zhou, Y. Shi, X. Qian, M. Alexander, X. Zhao, S. Mendez, R. Yang, L. Qu and G. Yu, *Nat Nanotechnol*, 2018, **13**, 489-495.
5. Z. Deng, J. Zhou, L. Miao, C. Liu, Y. Peng, L. Sun and S. Tanemura, *Journal of Materials Chemistry A*, 2017, **5**, 7691-7709.
6. S. Mao, M. A. H. Johir, C. Onggowarsito, A. Feng, L. D. Nghiem and Q. Fu, *Materials Advances*, 2022, **3**, 1322-1340.
7. B. Yang, Z. Zhang, P. Liu, X. Fu, J. Wang, Y. Cao, R. Tang, X. Du, W. Chen, S. Li, H. Yan, Z. Li, X. Zhao, G. Qin, X. Q. Chen and L. Zuo, *Nature*, 2023, **622**, 499-506.
8. Y. Tan, H. Jin, S. S. Mao and S. Shen, *Carbon Neutrality*, 2023, **2**, 11.
9. S. Guo, Y. Zhang, H. Qu, M. Li, S. Zhang, J. Yang, X. Zhang and S. C. Tan, *EcoMat*, 2022, **4**, (2)e12179.
10. X. Li, J. Li, J. Lu, N. Xu, C. Chen, X. Min, B. Zhu, H. Li, L. Zhou, S. Zhu, T. Zhang and J. Zhu, *Joule*, 2018, **2**, 1331-1338.
11. X. Min, B. Zhu, B. Li, J. Li and J. Zhu, *Accounts of Materials Research*, 2021, **2**, 198-209.
12. X. Liang, X. Zhang, Q. Huang, H. Zhang, C. Liu and Y. Liu, *Solar Energy*, 2020, **208**, 778-786.
13. Y. Guo, X. Zhou, F. Zhao, J. Bae, B. Rosenberger and G. Yu, *ACS Nano*, 2019, **13**, 7913-7919.

14. Y. Guo, F. Zhao, X. Zhou, Z. Chen and G. Yu, *Nano Lett*, 2019, **19**, 2530-2536.
15. Y. Lu, D. Fan, Y. Wang, H. Xu, C. Lu and X. Yang, *ACS Nano*, 2021, **15**, 10366-10376.
16. L. Wu, B. Zhao, D. Gao, D. Jiao, M. Hu and G. Pei, *Carbon Neutrality*, 2023, **2**, 6.
17. C. Tian, C. Li, D. Chen, Y. Li, L. Xing, X. Tian, Y. Cao, W. Huang, Z. Liu and Y. Shen, *Journal of Materials Chemistry A*, 2021, **9**, 15462-15471.
18. W. Li, X. Li, W. Chang, J. Wu, P. Liu, J. Wang, X. Yao and Z.-Z. Yu, *Nano Research*, 2020, **13**, 3048-3056.
19. X. Meng, J. Yang, S. Ramakrishna, Y. Sun and Y. Dai, *Journal of Materials Chemistry A*, 2020, **8**, 16570-16581.
20. H. Su, J. Zhou, L. Miao, J. Shi, Y. Gu, P. Wang, Y. Tian, X. Mu, A. Wei, L. Huang, S. Chen and Z. Deng, *Sustainable Materials and Technologies*, 2019, **20**, e00095.
21. F. Dixit, K. Zimmermann, R. Dutta, N. J. Prakash, B. Barbeau, M. Mohseni and B. Kandasubramanian, *Journal of Hazardous Materials*, 2022, **423**, 127050.
22. P. Ranjan, J. M. Lee, P. Kumar and A. Vinu, *Adv Mater*, 2020, **32**, e2000531.
23. Y. Hu, Y. Yin, S. Li, H. Zhou, D. Li and G. Zhang, *Nano Letters*, 2020, **20**, 7619-7626.
24. Z. Zhang, A. J. Mannix, X. Liu, Z. Hu, N. P. Guisinger, M. C. Hersam and B. I. Yakobson, *Science Advances*, 2019, **5**, eaax0246.
25. X. Liu, Q. Li, Q. Ruan, M. S. Rahn, B. I. Yakobson and M. C. Hersam, *Nature Materials*, 2021, **21**, 35-40.
26. A. J. Mannix, X.-F. Zhou, B. Kiraly, J. D. Wood, D. Alducin, B. D. Myers, X. Liu, B. L. Fisher, U. Santiago, J. R. Guest, M. J. Yacaman, A. Ponce, A. R. Oganov, M. C. Hersam and N. P. Guisinger, *Science*, 2015, **350**, 1513-1516.
27. B. Feng, J. Zhang, Q. Zhong, W. Li, S. Li, H. Li, P. Cheng, S. Meng, L. Chen and K. Wu, *Nature chemistry*, 2016, **8**, 563-568.
28. H. Li, L. Jing, W. Liu, J. Lin, R. Y. Tay, S. H. Tsang and E. H. T. Teo, *ACS Nano*, 2018, **12**, 1262-1272.
29. H. Lin, H. Shi, Z. Wang, Y. Mu, S. Li, J. Zhao, J. Guo, B. Yang, Z.-S. Wu and F. Liu, *ACS Nano*, 2021, **15**, 17327–17336.
30. T. T. Xu, J.-G. Zheng, Wu, A. W. Nicholls, J. R. Roth, D. A. Dikin and R. S. Ruoff, *Nano Letters*, 2004, **4**, 963-968.
31. G. Tai, T. Hu, Y. Zhou, X. Wang, J. Kong, T. Zeng, Y. You and Q. Wang, *Angewandte Chemie International Edition*, 2015, **54**, 15473-15477.
32. D. Ma, J. Zhao, J. Xie, F. Zhang, R. Wang, L. Wu, W. Liang, D. Li, Y. Ge, J. Li, Y. Zhang and H. Zhang, *Nanoscale Horizons*, 2020, **5**, 705-713.
33. A. L. James and K. Jasuja, *RSC Advances*, 2017, **7**, 1905-1914.
34. Y. Feng, R. Qi, L. Jiang, Q. Huang, T. Li, G. Liu, W. Li, W. Yan, Z. Zhang and Z. Wang, *Materials*, 2021, **14**, 1319.
35. S. Mao, C. Onggowarsito, A. Feng, S. Zhang, Q. Fu and L. D. Nghiem, *Journal of Materials Chemistry A*, 2023, **11**, 858-867.
36. C. Li, B. Zhu, Z. Liu, J. Zhao, R. Meng, L. Zhang and Z. Chen, *Chemical Engineering Journal*, 2022, **431**, 134224.
37. G. I. Andrade, E. F. Barbosa-Stancioli, A. A. P. Mansur, W. L. Vasconcelos and H. S. Mansur, *Journal of Materials Science*, 2007, **43**, 450-463.
38. H. S. Mansur, C. M. Sadahira, A. N. Souza and A. A. P. Mansur, *Materials Science and Engineering: C*, 2008, **28**, 539-548.
39. S. Gupta, T. J. Webster and A. Sinha, *J Mater Sci Mater Med*, 2011, **22**, 1763-1772.
40. X. Zhou, F. Zhao, Y. Guo, B. Rosenberger and G. Yu, *Science Advances*, 2019, **5**, eaaw5484.
41. Y. Zhang and S. C. Tan, *Nature Sustainability*, 2022, **5**, 554-556.

42. Y. Tu, J. Zhou, S. Lin, M. Alshrah, X. Zhao and G. Chen, *Proceedings of the National Academy of Sciences*, 2023, **120**, e2312751120.
43. L. Zhang, B. Tang, J. Wu, R. Li and P. Wang, *Advanced Materials*, 2015, **27**, 4889-4894.
44. Y. Xu, J. Xu, J. Zhang, X. Li, B. Fu, C. Song, W. Shang, P. Tao and T. Deng, *Nano Energy*, 2022, **93**, 106882.
45. Y. Guo, X. Zhao, F. Zhao, Z. Jiao, X. Zhou and G. Yu, *Energy & Environmental Science*, 2020, **13**, 2087-2095.
46. T. Gao, Y. Wang, X. Wu, P. Wu, X. Yang, Q. Li, Z. Zhang, D. Zhang, G. Owens and H. Xu, *Science Bulletin*, 2022, **67**, 1572-1580.
47. World Health Organization, *Calcium and Magnesium in Drinking Water Public Health Significance*, World Health Organization, Geneva, Switzerland, 2009.
48. World Health Organization, *Potassium in Drinking-Water: Background Document for Development of WHO Guidelines for Drinking Water Quality*, World Health Organization, Geneva, Switzerland, 2009.